Rockefeller University
Report No. COO-2232A-67

RESULTS ON CORRELATIONS AND JETS IN HIGH TRANSVERSE MOMENTUM p-p COLLISIONS AT THE CERN ISR

CERN[1]-Columbia[2]-Oxford[3]-Rockefeller[4] (CCOR) Collaboration

A.L.S. Angelis[3], B.J. Blumenfeld[2], L. Camilleri[1], T.J. Chapin[4], R.L. Cool[4], C. del Papa[1], L. Di Lella[1], Z. Dimčovski[4], R.J. Hollebeek[2], D. Levinthal[2], L.M. Lederman[2], J.T. Linnemann[4], L. Lyons[3], N. Phinney[3], B.G. Pope[1*)], S.H. Pordes[1], A.F. Rothenberg[4**)], A.M. Segar[3], J. Singh-Sidhu[1], A.M. Smith[1], M.J. Tannenbaum[4], R.A. Vidal[2***)], J. Wallace-Hadrill[3], T.O. White[3†)] and J.M. Yelton[3]

ABSTRACT

A large solid-angle apparatus consisting of a superconducting solenoid magnet, cylindrical drift chambers, and two arrays of lead-glass counters is used to examine particles associated with a high transverse momentum trigger in pp interactions at the CERN ISR.

The trigger is given by energy deposition in the lead-glass arrays centred at 90°. Results on particle correlations and on jets are presented for interactions at $\sqrt{s}$ = 62.4 GeV and in the trigger transverse momentum range $3 < p_T < 11$ GeV/c.

Submitted to the
XIX International Conference on High Energy Physics
Tokyo, August 1978

Geneva - 29 September 1978

*) Present address: Physics Dept., Princeton University, NJ, USA.
**) Present address: CERN, Geneva, Switzerland.
***) Present address: Stanford Linear Acc. Center, Stanford, CA, USA.
†) Present address: Cavendish Laboratory, University of Cambridge, U.K.

DISCLAIMER

1. Introduction

The observation of unexpectedly high hadron-hadron inclusive production at large transverse momentum several years ago [1] has led to considerable experimental and theoretical effort to understand these phenomena. Some of the principal sources of data are the experiments that investigate the correlations between the particles produced in such a high transverse momentum collision. This paper reports the preliminary results obtained by the CCOR Collaboration at the CERN Intersecting Storage Rings (ISR).

Previous correlation studies [2] at the CERN ISR have helped the development of a jet theory of high-p_T interactions. Each experiment has improved on its predecessors by adding momentum measurement, improving the solid angle, or raising the trigger energy. Momentum measurement is necessary to investigate resonance structure and to study the correlation effects as a function of the momentum of particles. A large solid angle is needed to contain the event in the apparatus and to demonstrate that the effects observed are independent of the acceptance cut of the apparatus. A high trigger energy is desirable because the strength of the correlations (the jet-like nature of the events) is expected to increase with the trigger transverse momentum. Unfortunately, no single experiment has succeeded in doing all three. In particular, no apparatus has had momentum measurement over the full azimuth. The experiment discussed in this paper goes further by combining a high-p_T lead-glass trigger covering $\sim$ 2 sr, with charged particle momentum measurement over the full azimuth and a limited rapidity

interval. The lead-glass trigger system together with the improved luminosity of the ISR now allows study of triggers with $p_T \sim 10$ GeV/c, as compared to previous experiments with $p_T \sim 4$ GeV/c.

2. Apparatus

The apparatus (Fig. 1) consists of a 1.5 tesla aluminium-stabilized superconducting solenoid which contains cylindrical drift chambers surrounding the interaction region. In addition, there are two walls of lead-glass total absorption Čerenkov counters, each covering a solid angle of ~ 1 sr.

The solenoid has a usable cylindrical volume 170 cm long with a radius of 70 cm. Its field of 1.5 tesla is uniform to 1.5% over the entire solid angle covered by the four cylindrical drift-chamber modules (DCM1-DCM4). Each module contains two layers of drift chambers. They are of the adjustable electric field design to allow for compensation of magnetic field forces over drift distances up to 2.2 cm. The 580 sense wires of this system are parallel to the magnetic field, and the drift time is used to measure the ϕ coordinates of charged tracks passing through the chambers. This is the coordinate that requires the most accuracy, as it determines the transverse momentum p_T of the tracks. The left-right sense wire ambiguity in each module is partially resolved by the angular offset of the outer gap's sense wires with respect to those of the inner by half the sense-sense angle. Delay lines are glued to one of the cathode planes facing each of the 580 sense wires. An avalanche on the sense wire induces a pulse on the delay line. The z coordinate (along the solenoid axis) can then be extracted from the

times of arrival of this induced pulse at the two ends of the delay line. Thus, by providing pairs of ϕ and z coordinates, the system reduces the off-line computing load by eliminating the need for ϕ and z matching. In addition, the solenoid contains a barrel hodoscope of 32 counters ("A") between DCM1 and DCM2 which are used to give a timing signal for each event and to check the validity of tracks. More information on the solenoid [3] and the chambers [4] can be found elsewhere.

The detector is triggered by energy deposition in either of the two walls of lead glass [5] located just outside the thin-walled ($\sim$ 1 r.l.) region of the solenoid at a distance of 140 cm from the intersection region. Each wall consists of 168 blocks arranged into a 12 × 14 array. The blocks are 15 × 15 × 40 cm (17 r.l.). They are calibrated using a monoenergetic electron beam at the CERN Proton Synchrotron (PS). This calibration is monitored by recording the pulse height of the light emitted by small NaI crystals, doped with ^{241}Am, which are glued to each block. Further checks on the calibration are provided by monitoring the magnitude of the pulse-height peak produced by charged hadrons traversing an entire block and by measuring the π^0 mass in events containing two well-separated photons. Both of these checks are made with the glass withdrawn to 350 cm from the intersection region. Two 12-counter hodoscopes ("B") located between the magnet and the glass are used to sense the showering of particles in the solenoid coil and to allow correction for the energy loss due to this effect.

3. Analysis and cuts

Data have been taken with the ISR operating at $\sqrt{s}$ = 62.4 and at luminosities up to 4×10^{31} cm^{-2} s^{-1}. They can be divided into four groups with different centre-of-mass trigger thresholds: i) zero -- the trigger is provided by a pulse from any one of the A counters; ii) $p_T > 3$ GeV/c; iii) $p_T > 5$ GeV/c; and, iv) $11 > p_T > 7$ GeV/c.

Tracks are reconstructed (≥ 5 points) and vertices are found for all events. Events whose tracks do not form a vertex in the "diamond" intersection region of the two beams are rejected. High p_T events with less than four A-counters are rejected to reduce background at very high p_T. Tracks are discarded if they do not point to the vertex or if they do not have A-counter signals in time (±15 ns) with the event. The track reconstruction efficiency is $\sim$ 80%; the vertex cut removes 10% of the good events from the sample. The r.m.s. momentum resolution is

$$\Delta p_T/p_T \sim \sqrt{(0.02)^2 + (0.07\ p_T)^2} \qquad (p_T \text{ in GeV/c}) ,$$

where the first term is due to multiple coulomb scattering and the second results from a $\sim$ 500 μ drift-chamber resolution. The track reconstruction losses are predominantly due to drift chamber inefficiency. The inefficiency of the vertex cut is due to track losses and to the extrapolation errors due to drift chamber resolution. The momentum resolution is for a long running-period early in the operation of the system, and includes effects of uncertainties in the chamber alignment as well as in the time-distance relations in the chambers. It is also influenced by the ϕ ambiguities

occurring when only one point out of the two in a module is present, and by the shorter lever arm available for tracks which lose both points in DCM1 or DCM4.

The energy deposited in the glass is required to come from clusters not larger than 3 × 3 blocks. It is corrected for the angle between the incoming photon(s) and the glass, and for the energy loss in the solenoid wall using information from the associated B counters. The r.m.s. energy resolution of the lead glass is $\Delta E/E \sim 0.05 + 0.04/\sqrt{E}$. There is a systematic uncertainty of $\sim$ 5% in the absolute energy calibration of the lead glass.

The laboratory momenta of all particles are transformed to the centre-of-mass system assuming that the particles are pions. Pseudo-rapidities $\{\eta = -\ln [\tan (\theta/2)]\}$ are calculated for each particle. The trigger particle is defined to be the neutral particle with the maximum p_T. This p_T is required to be above the threshold cut for the data set. Events in which a charged particle strikes the glass within 28 cm of the trigger cluster are rejected. This cut eliminates clusters whose energy is partly from a charged particle. It also rejects high-momentum electrons from Dalitz decay or conversion of neutrals in the vacuum pipe and chambers which would otherwise be considered as associated hadrons. This cut biases the study of correlations on the same side as the trigger. The correlations on the side opposite to the trigger are not affected by such a cut. Acceptance cuts are applied so as to make the apparatus symmetric in the centre-of-mass system. The cuts used for the trigger particle and the associated particles are given in Table I. Table II contains the number of events and tracks passing these cuts.

For this preliminary analysis, no corrections have been made for efficiency or momentum and energy resolution.

4. Charged particle correlations

One of the simplest correlations is the azimuthal correlation of charged tracks with the trigger particle. These are shown in $dn/d\phi$ plots (Fig. 2) for five 1 GeV/c bands of charged particle transverse momentum, where $dn/d\phi$ is the average number of tracks per unit azimuth per event with trigger $p_{T\,t} > 7$ GeV/c. The azimuth of a track is measured relative to that of the trigger. The plot is split into two halves for the same ($|\phi| < \pi/2$, Fig. 2a) and away ($|\phi - \pi| < \pi/2$, Fig. 2b) sides. Strong correlation peaks on top of flat backgrounds can be seen in all plots. In each band the level of the flat background is similar to that found in the zero threshold trigger. The same-side correlation peaks shown here have been diminished from their true values, and their shapes have been changed because of the cut on track-to-cluster distance explained in the previous section. The width of the away-side peak shrinks with increasing charged particle p_T, as is expected in almost all models. This will be discussed later using the variable p_{out}. The FWHM $\sim$ 1 radian at low p_T shows that the correlation enhancement extends over almost all of the away side. The away-side azimuthal correlation for all tracks with $p_T > 0.3$ GeV/c is shown for four 1 GeV/c bands of trigger $p_{T\,t}$ (Fig. 3). The peak becomes higher and narrower as the trigger $p_{T\,t}$ increases.

Another possible correlation is that between the rapidity of the away-side charged particle and the trigger. Historically no effect

has been seen. This remains true in this experiment as shown in the plots of $dn/d(\eta_{track} - \eta_{trigger})$ (Fig. 4a). The triangular shape observed is that expected from the folding together of two independent flat η distributions ($|\eta| < 0.5$ for the trigger and $|\eta| < 0.7$ for charged particles). A plot of $dn/d(\eta_{track} + \eta_{trigger})$ has the same shape. A rapidity correlation can be observed between charged particles on the away side and the maximum p_T particle on the away side (leader). This was one of the earliest observed effects which supported a "jet" picture of high p_T interactions. It is shown in the $dn/d(\eta_{track} - \eta_{leader})$ plot (Fig. 4b). This correlation is also observed to shrink in width as a function of the p_T track.

The information from all four data sets can be compared by studying the variation with track p_T and trigger $p_{T\,t}$ of the following correlation functions defined for the away side and calculated using $dn/d\phi$ distribution of the type shown in Fig. 2b:

$$\bar{f}(p_T,\ p_{T\,t}) = \frac{\Delta n}{\Delta p_T\ \Delta\eta\ \Delta\phi}\ (p_T,\ p_{T\,t}) = \frac{1}{\Delta p_T\ 1.4\ \pi} \int_{\pi/2}^{3\pi/2} d\phi\ \frac{dn}{d\phi}\ (\phi)\ ,$$

$$f_{max}\ (p_T,\ p_{T\,t}) = \frac{1}{\Delta p_T\ 1.4}\ \frac{dn}{d\phi}\ (\phi = \pi),\quad \Delta p_T = 1.0\ \text{GeV/c}\ .$$

They are shown in Figs. 5a and 5b, respectively; $\bar{f}(p_T,\ p_{T\,t})$ shows how the number of charged particles averaged over the entire away side varies as a function of their p_T for trigger transverse momentum above $p_{T\,t}$, while $f_{max}(p_T,\ p_{T\,t})$ shows the changes in the peak number of particles. Previous experiments with small azimuthal acceptance could only measure f_{max}. The strong correlation increasing with

p_T and $p_{T\,t}$ has been seen before but not for such a wide range of $p_{T\,t}$. The average multiplicity $\bar{F}(p_{T\,t})$ of tracks ($p_T > 0.3$ GeV/c) per unit rapidity and unit azimuth on the away side is derived from the $dn/d\phi$ distributions of Fig. 3 and is plotted in Fig. 5c. Figure 5d shows the multiplicity $F_{max}(p_{T\,t})$ of tracks ($p_T > 0.3$ GeV/c), per unit rapidity and unit azimuth at $\phi = \pi$, which is the maximum of the correlation on the away side. The plot of $\bar{F}$ shows that the multiplicity is rising as a function of $p_{T\,t}$. The fact that F_{max} rises faster than $\bar{F}$ shows that the azimuthal peak must be shrinking as a function of $p_{T\,t}$.

It has become standard practice to study dn/dx_E and $\langle|p_{out}|\rangle$ distributions as a function of x_E. These variables are defined in Fig. 6. The results for $\langle|p_{out}|\rangle$ (Fig. 7a) do not appear to scale in x_E for different $p_{T\,t}$. Agreement with previous results [6] is reasonable for the low threshold data. It can also be seen that at constant p_T (Fig. 7b), $\langle|p_{out}|\rangle$ is higher for low $p_{T\,t}$. It should be noted that these plots have not been corrected for the effects due to momentum resolution.

In parton models p_{out} is often thought of as being composed of two contributions, one from the transverse momentum of the two partons that enter the hard scattering process k_T, and the other from the transverse momentum given to a particle during the fragmentation of its parent parton after the scattering q_T. In this picture

$$\langle|p_{out}|\rangle = \sqrt{\langle k_T\rangle^2\, x_E^2 + \frac{1}{2}\langle q_T\rangle^2\,(1 + x_E^2)}\ .$$

One of the striking features of previous experiments [6] was the increase of $\langle |p_{out}| \rangle$ with x_E, which led to the introduction of models in which $\langle k_T \rangle$ was forced to be much greater than the originally expected value of $\langle k_T \rangle \sim 0.3$ GeV/c. In order to explain the p_T imbalance in high-mass electron pair production at FNAL [7], a value of $\langle k_T \rangle \sim 0.85$ GeV/c has been used [8]. The results shown in Fig. 7 suggest an even larger value of $\langle k_T \rangle$ and also a dependence of $\langle k_T \rangle$ on the trigger $p_{T\,t}$.

The dn/dx_E spectra (Fig. 8) appear to scale in x_E. However, it is important to remember that these distributions have not been corrected for momentum resolution. To study these correlations further, the azimuthal acceptance is restricted to a region $|\phi - \pi| < \pi/3$. As can be seen from the azimuthal distributions (Fig. 2), such a cut contains the correlated peak. A distribution of the total charged x_E, the sum of the x_E's of all of the charged tracks, for three 1 GeV/c intervals of trigger $p_{T\,t}$ is shown in Fig. 9. No cuts are made on the direction or magnitude of the sum of the momenta. Thus the plot shows the distribution of balancing momentum that falls in a fixed rapidity interval independent of the direction of the away-side jet. The x_E scaling of this distribution is fairly good in the interval considered, but again no corrections are made for momentum resolution.

Same-side charged particle correlations with the trigger are also studied in a restricted ϕ region ($|\phi| < \pi/3$) which contains the correlation peak. In order to be able to use more of the same-side correlated charged particles, tracks pointing to within 20 cm of the trigger energy in the lead glass are excluded, but the event

is still used. This cut excludes a $\sim$ 0.05 sr disk around the trigger in the centre-of-mass system. The trigger neutral is required to have $|\eta| < 0.4$ to ensure a large solid angle for tracks accompanying it. The single-particle transverse momentum distribution (Fig. 10) is found to be almost independent of the trigger $p_{T\,t}$ for all three sets of data. Summing the x_E of all charged tracks in the same-side region and averaging over all events gives the mean values of the total charged x_E as a function of trigger $p_{T\,t}$ (Fig. 11). The accompanying momentum on the same side is a small fraction of $p_{T\,t}$. This is a demonstration of the trigger bias introduced by a neutral cluster trigger requirement.

In the two remaining 60° regions, $\pi/3 < |\phi| < 2\pi/3$, which are outside the correlation enhancements, the shape of the single-particle momentum spectrum can be seen to differ only slightly from the zero threshold spectrum (Fig. 12).

5. Correlations to a vector sum

The correlations between away-side particles provide an important test of the constituent hard-scattering model of high p_T particle production. The constituent should fragment into particles whose momenta are distributed symmetrically about the constituent's momentum vector. In this analysis, the vector sum of the observed charged particles' momenta is used to approximate this vector. Missing neutral and undetected charged particles can affect the direction and magnitude of the measured total momentum, hence the results are only suggestive and not quantitative.

The vector sum is constructed from the charged particles on the away side with $|\phi-\pi| \leq \pi/3$ and $|\eta| < 0.7$. Events are selected which have $|\eta_{sum}| < 0.3$ and $p_{T\,sum} > 3$ GeV/c. The first cut ensures that events are centred in the apparatus. The second cut eliminates events containing only low-energy spectator hadrons. Only data with $p_{T\,t} > 7$ GeV/c are used.

The fragmentation about the axis is defined in terms of two variables $|p_{out\,\phi}|$ and $|p_{out\,\theta}|$ (Fig. 13). The mean values for these quantities are plotted in Fig. 14 as a function of the p_T of the particle. They are approximately equal and limited to about 0.35 GeV/c. The dip at 3 GeV is due to the threshold for events with only one away-side particle which satisfies the cuts and gives $p_{out} = 0$.

The data can be compared with curves generated by a Monte Carlo simulation, which are shown on the same plots. For the simulation, a trigger p_T is picked from the observed distribution. An away-side multiplicity is chosen according to the distribution of multiplicities seen for centred events ($\langle n_{ch} \rangle = 3.5$). Charged particle momenta are selected from the measured p_T distribution associated with the chosen trigger p_T. For $p_{out\,\theta}$, the θ of the track is picked from a flat distribution since no θ correlation is observed. In $p_{out\,\phi}$, there are two curves: in the upper curve ϕ is picked according to a flat distribution; in the lower curve ϕ is picked according to the five $dn/d\phi$ plots of Fig. 2.

The $\langle |p_{out\,\phi}| \rangle$ and $\langle |p_{out\,\theta}| \rangle$ from the Monte Carlo simulation rise to values of 0.9 and 0.75 GeV/c, respectively. The difference between these values and the data demonstrates that the maximum

values seen in the data are not due to the limitations of the acceptance used in this analysis. Inclusion of the ϕ correlations lowers the $\langle |p_{out\,\phi}| \rangle$ to 0.55 GeV/c, which is still significantly higher than the data. The fact that the Monte Carlo curves also level off (though at a higher-track p_T) reflects the degree to which a single high-momentum particle dominates the vector sum. This occurs because the multiplicities are low, and the other particles contributing to the sum have a steeply falling momentum spectrum. The fact that the observed p_{out} values are smaller than those formed with the Monte Carlo simulation indicates that the correlation between away-side particles is stronger than that indicated by their independent correlations to the trigger.

6. Conclusions

The following conclusions can be made from the preliminary results shown for the charged particles produced in association with a high-p_T neutral in p-p collisions at $\sqrt{s}$ = 62.4.

i) The azimuthal correlation of charged particles with a triggering neutral forms two broad peaks at $\phi = 0$ and $\phi = \pi$.

ii) There is no rapidity correlation of away-side charged particles with a neutral trigger, even at the highest trigger p_T.

iii) There is a rapidity correlation of away-side particles relative to the highest p_T particle on the away side.

iv) The width of the away-side azimuthal correlation enhancement decreases with charged particle p_T.

v) The strength of the away-side azimuthal enhancement increases with trigger p_T.

vi) $\langle |p_{out}| \rangle$ increases as a function of x_E and trigger p_T (for fixed x_E) reaching values above 1 GeV/c. (Note: no correction for momentum resolution has been made.)

vii) dn/dx_E appears to scale in x_E over a wide range of trigger p_T. (Note: no correction for momentum resolution has been made.) The same is true for $dN/d(\Sigma x_E)$.

viii) The hadrons in the same-side correlation enhancement have a momentum spectrum which appears to be independent of trigger p_T. The fraction of the energy in charged hadrons accompanying the trigger decreases with trigger p_T.

ix) The shape of the spectrum of tracks outside of the two azimuthal correlation enhancements is the same as that for zero threshold triggers.

x) Reconstructing an away-side jet using only the observed charged particles shows fragmentation that is symmetric about the jet axis.

REFERENCES

1. Alper, B. et al., Phys. Letters 44B, 521 (1973).
Banner, M. et al., Phys. Letters 44B, 537 (1973).
Büsser, F.W. et al., Phys. Letters 46B, 471 (1973).

2. Finocchiaro, G. et al., Phys. Letters 50B, 396 (1974).
Büsser, F.W. et al., Phys. Letters 51B, 310 (1974).
Eggert, K. et al., Nuclear Phys. B98, 73 (1975).
Büsser, F.W. et al., Nuclear Phys. B106, 1 (1976).
Darriulat, P. et al., Nuclear Phys. B107, 429 (1976).
Della Negra, M. et al., Nuclear Phys. B127, 1 (1977).
Albrow, M. et al., Nuclear Phys. B135, 461 (1978).
Bøggild, H., Proc. 8th Symposium on Multiparticle Dynamics, Kaysersberg, France, 1977 (Centre de Recherches nucléaires, Strasbourg, 1977), p. B-1.

3. Morpurgo, M., Cryogenics 17, 89 (1977).

4. Camilleri, L. et al., A system of cylindrical drift chambers in a superconducting solenoid, Paper presented at the Wire Chamber Conference, Vienna, 1978, to be published in Nuclear Instrum. Methods.

5. Beale, J.S. et al., Nuclear Instrum. Methods 117, 50 (1974).

6. Della Negra, M. et al., Nuclear Phys. B127, 1 (1977).

7. Herb, S.W. et al., Phys. Rev. Letters 39, 252 (1977).
Innes, W.R. et al., Phys. Rev. Letters 39, 1246 (1977).

8. Feynman, R.P. et al., CALT-68-651 (1978).

Table I

Acceptance cuts for particles

	p_T	Pseudo-rapidity	Azimuth
Charged	$p_T > 0.3$	$\|\eta\| < 0.7$	No cut
Neutral cluster	$p_T >$ threshold	$\|\eta\| < 0.5$	$\|\phi\| < 0.47$ $\|\phi-\pi\| < 0.47$

Table II

Data Group

Centre-of-mass p_T threshold	None	3 GeV/c	5 GeV/c	7 GeV/c
Average trigger p_T		3.76 GeV/c	5.8	8.0
Luminosity	10^{30}	2.4×10^{34} cm^{-2}	5.6×10^{35}	1.6×10^{37}
No. of events	19,499	10,000	6,600	13,100
Tracks/event	3.2 ± 0.02	6.39 ± 0.02	6.58 ± 0.02	6.74 ± 0.02
$\frac{\text{Tracks}}{\text{Event}}$ (same side) in acceptance region	0.77 ± 0.006	1.15 ± 0.01	1.18 ± 0.01	1.16 ± 0.01
$\frac{\text{Tracks}}{\text{Event}}$ (away side) in acceptance region	0.77 ± 0.006	1.85 ± 0.01	2.23 ± 0.02	2.52 ± 0.01

Figure captions

Fig. 1 : a) A view of the apparatus normal to the solenoid axis. The lead-glass walls were 140 cm from the centre of the solenoid for the data discussed in this paper.

b) Top view of the apparatus.

Fig. 2 : Charged particle correlations.

a) Same-side azimuthal correlation of charged particles relative to the triggering neutral.

b) Away-side azimuthal correlation of charged particles relative to the triggering neutral.

Five plots corresponding to 1 GeV/c intervals in p_T of the charged particle are shown. The data is for trigger p_T > 7 GeV/c.

Fig. 3 : Away-side azimuthal correlation of charged particles with p_T > 0.3 GeV/c relative to the triggering neutral. Four plots corresponding to 1 GeV/c intervals in $p_{T\,t}$ of the trigger are shown.

Fig. 4 : a) Rapidity correlation of away-side charged particles relative to the triggering neutral.

b) Rapidity correlations of charged particles in the away-side relative to the maximum p_T particle on that side. (The maximum p_T particle is not included in the plot.)

Five plots corresponding to 1 GeV/c intervals in p_T of the charged particle are shown. The data is for trigger p_T > 7 GeV/c.

Fig. 5 : Away-side charged particle correlation functions.

a) $\bar{f}$ as defined in the text plotted as a function of the charged particle p_T for the three sets of trigger $p_{T\,t}$ and the zero threshold sample.

b) f_{max} plotted as $\bar{f}$ above.

c) $\bar{F}$ plotted as a function of trigger $p_{T\,t}$ after integrating over charged particle $p_T > 0.3$ GeV/c.

d) F_{max} plotted as $\bar{F}$ in (c).

Fig. 6 : A diagram showing the definition of variables used to relate particles to the trigger.

Fig. 7 : a) and b) $\langle |p_{out}| \rangle$ of away-side charged particles relative to the trigger for the three sets of trigger $p_{T\,t}$.

Fig. 8 : dn/dx_E distribution of away-side charged particles relative to the neutral trigger for the three sets as above.

Fig. 9 : $dN/d(\Sigma x_E)$ distribution for away-side charged particles in $|\phi-\pi| < \pi/3$ relative to the neutral trigger for the three sets of trigger $p_{T\,t}$.

Fig. 10 : dn/dp_T distribution of same-side charged particles in $|\phi| < \pi/3$ for the three sets of trigger p_T. The zero threshold spectrum is also shown.

Fig. 11 : $\langle \Sigma x_E \rangle$ for same-side charged particles in $|\phi| < \pi/3$ as a function of trigger p_T.

Fig. 12 : dn/dp_T for charged particles in two azimuthal regions between the correlated ϕ peaks ($\pi/3 < |\phi| < 2\pi/3$). The zero threshold dn/dp_T spectrum is also shown.

Fig. 13 : Diagram showing the definition of variables used in the vector sum analysis.

Fig. 14 : a) $\langle |p_{out\,\phi}| \rangle$ of particles relative to the away-side vector sum. The two Monte Carlo predictions described in the text are shown.

b) $\langle |p_{out\,\theta}| \rangle$ particles relative to the away-side vector sum. The Monte Carlo prediction described in the text is shown.

The track p_T distributions used in the Monte Carlo did not extend beyond 5 GeV/c.

a)

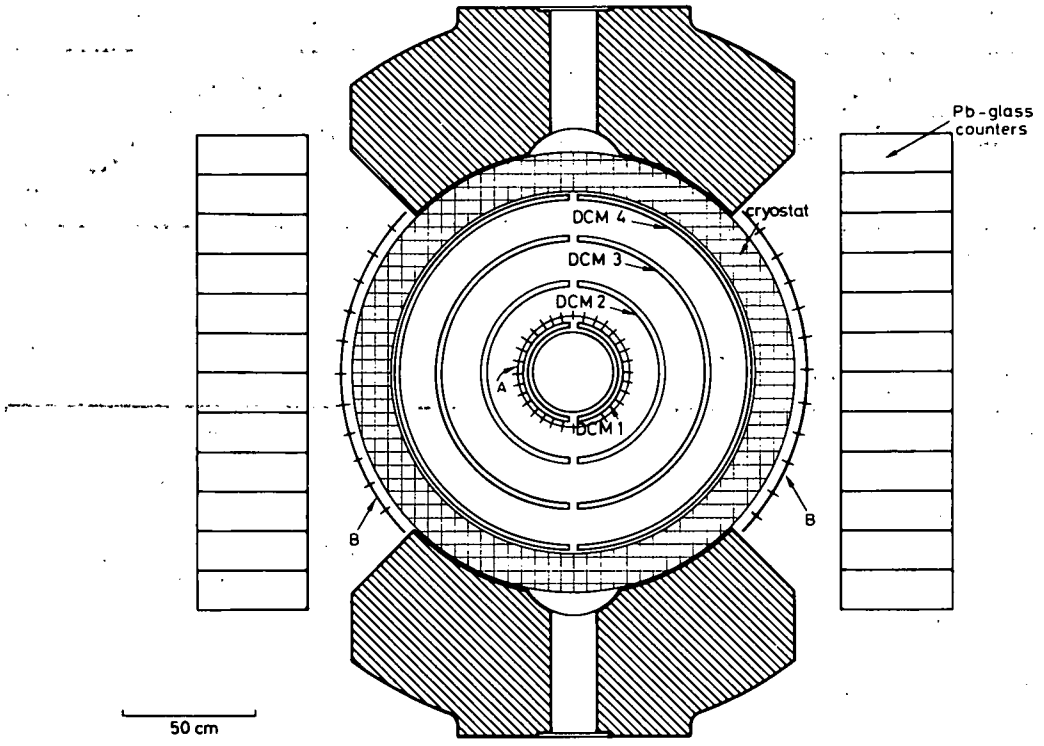
Pb-glass
counters
cryostat
DCM 4
DCM 3
DCM 2
DCM 1
A
B
B
50 cm

b)

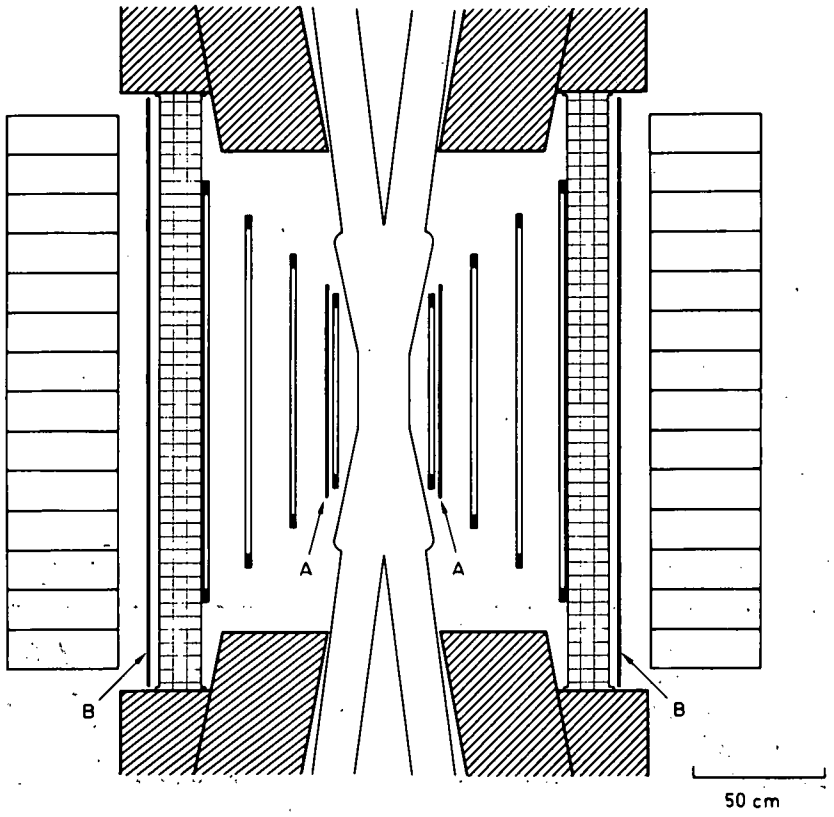
A
A
B
B
50 cm

Fig. 1

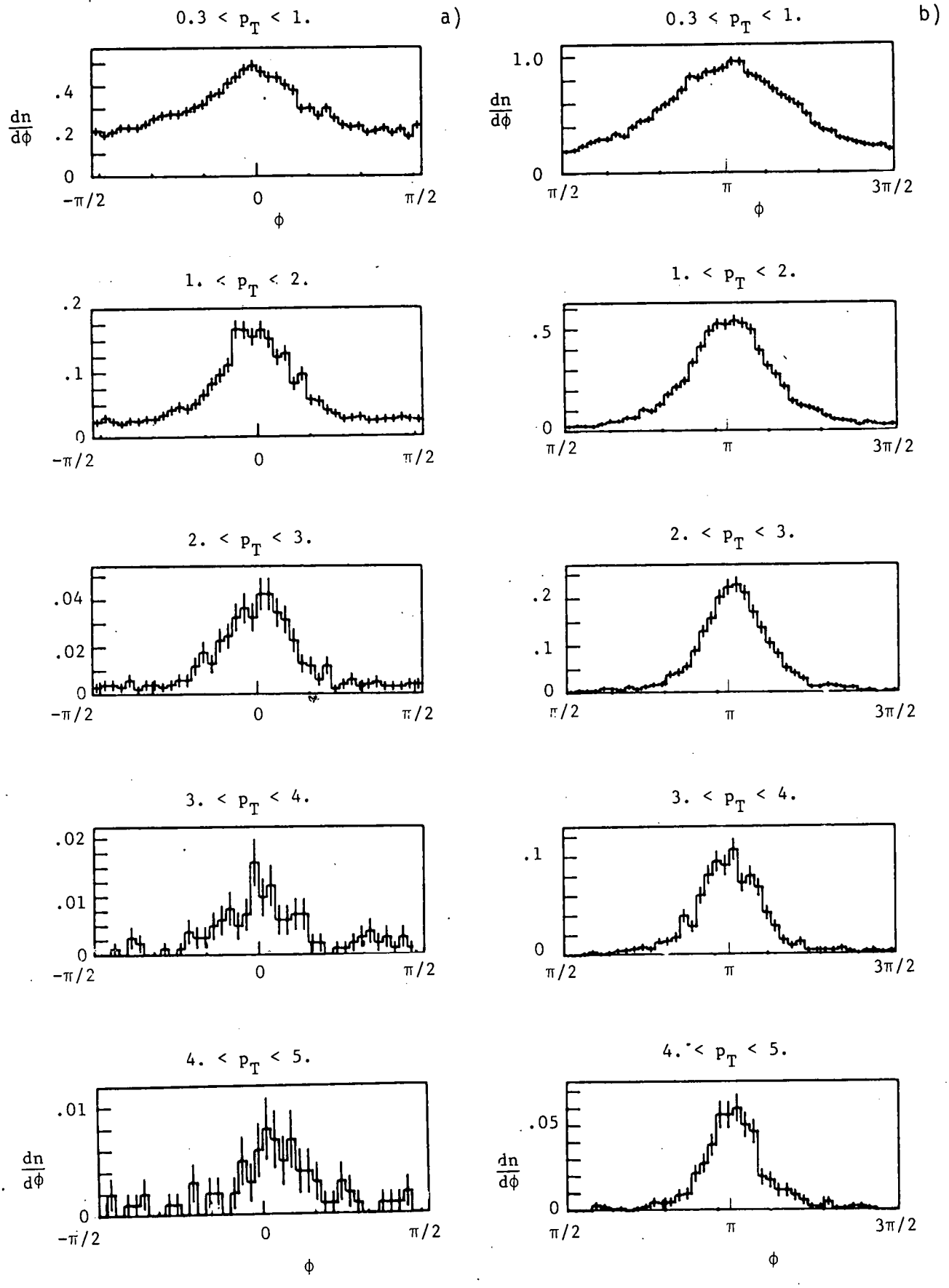

Fig. 2

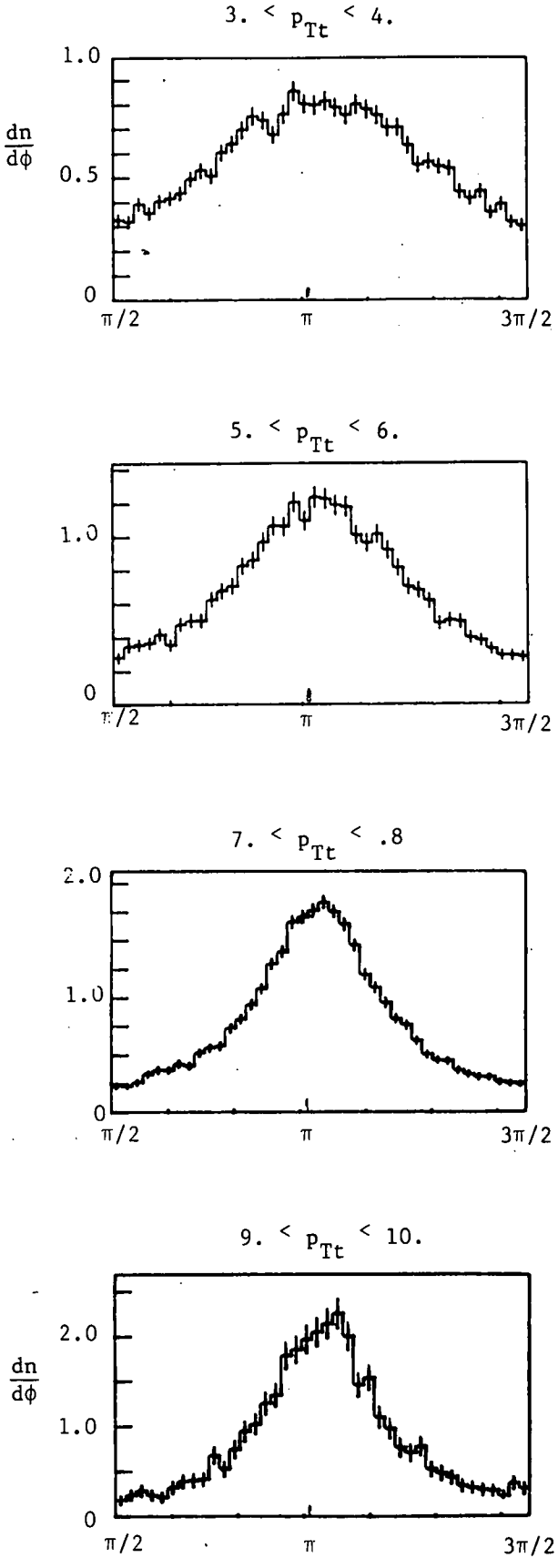
3. < p_{Tt} < 4.
$\frac{dn}{d\phi}$
1.0
0.5
0
π/2
π
3π/2
5. < p_{Tt} < 6.
1.0
0
π/2
π
3π/2
7. < p_{Tt} < .8
2.0
1.0
0
π/2
π
3π/2
9. < p_{Tt} < 10.
$\frac{dn}{d\phi}$
2.0
1.0
0
π/2
π
3π/2

Fig. 3

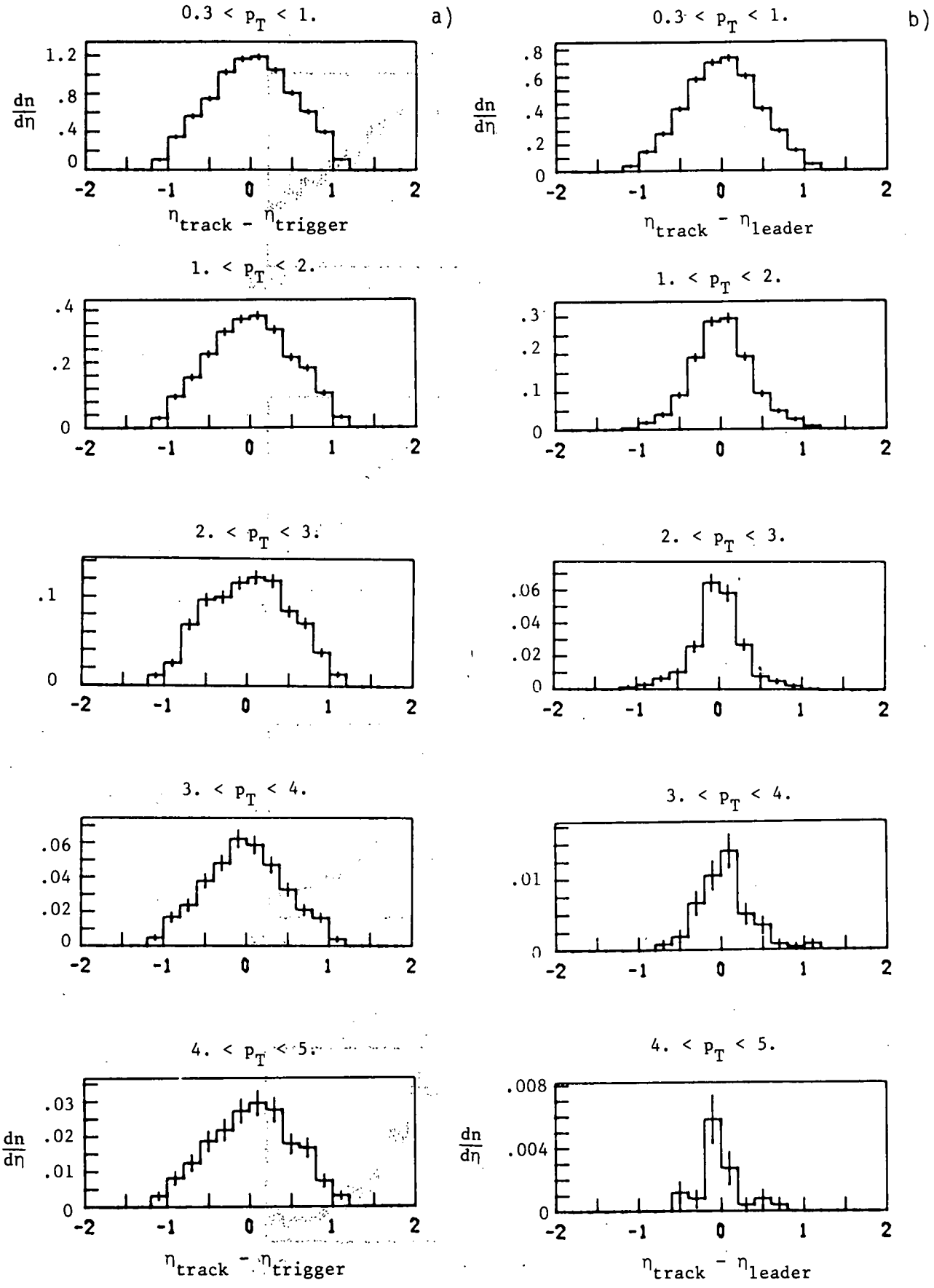
a)
b)
0.3 < p_T < 1.
1. < p_T < 2.
2. < p_T < 3.
3. < p_T < 4.
4. < p_T < 5.
$\frac{dn}{d\eta}$
$\eta_{track} - \eta_{trigger}$
$\eta_{track} - \eta_{leader}$

Fig. 4

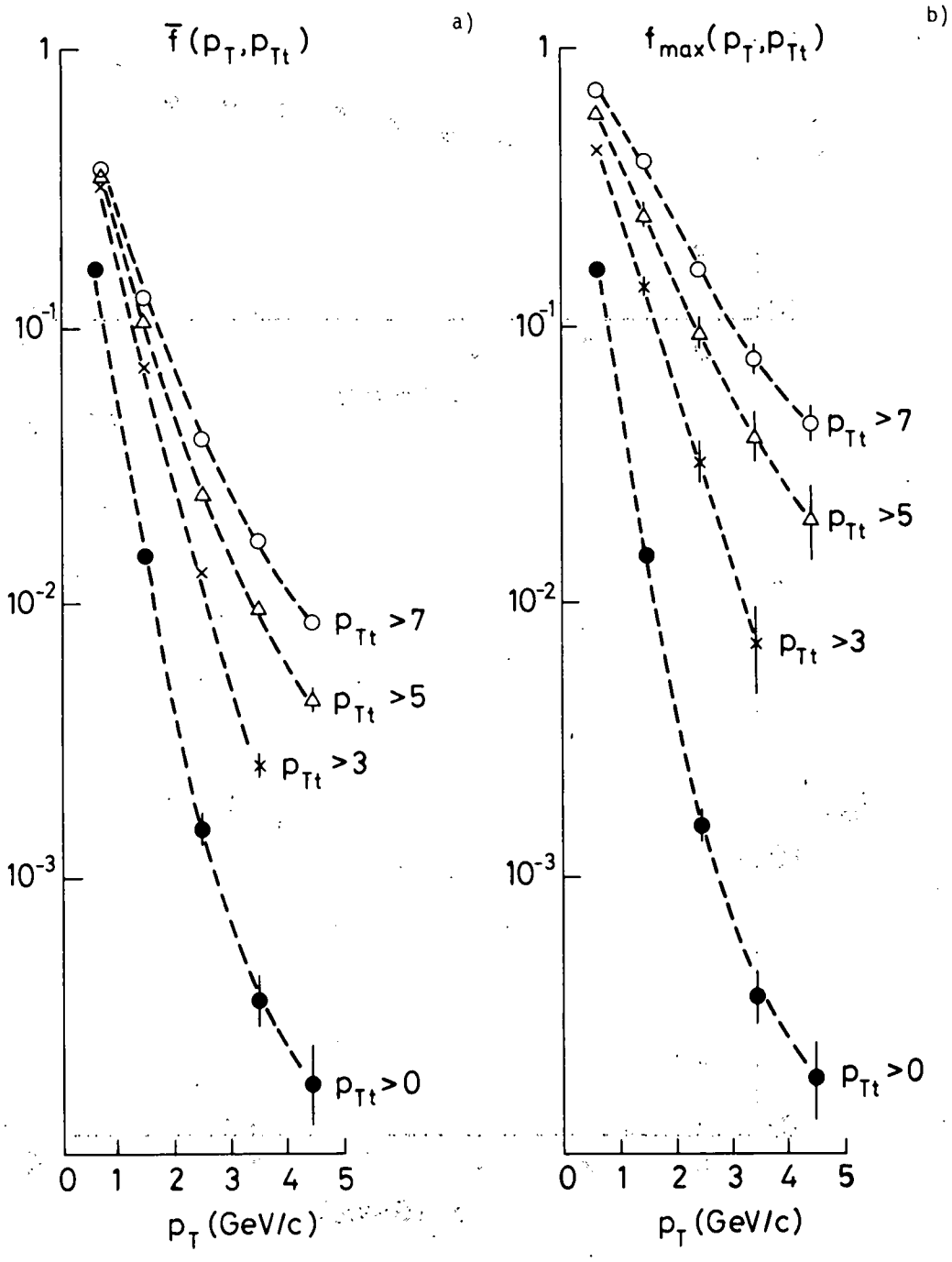
a)
$\bar{f}(p_T, p_{Tt})$
1
10^{-1}
10^{-2}
10^{-3}
$p_{Tt}>7$
$p_{Tt}>5$
$p_{Tt}>3$
$p_{Tt}>0$
0 1 2 3 4 5
p_T (GeV/c)
b)
$f_{max}(p_T, p_{Tt})$
1
10^{-1}
10^{-2}
10^{-3}
$p_{Tt}>7$
$p_{Tt}>5$
$p_{Tt}>3$
$p_{Tt}>0$
0 1 2 3 4 5
p_T (GeV/c)

Fig. 5 (a) (b)

c)

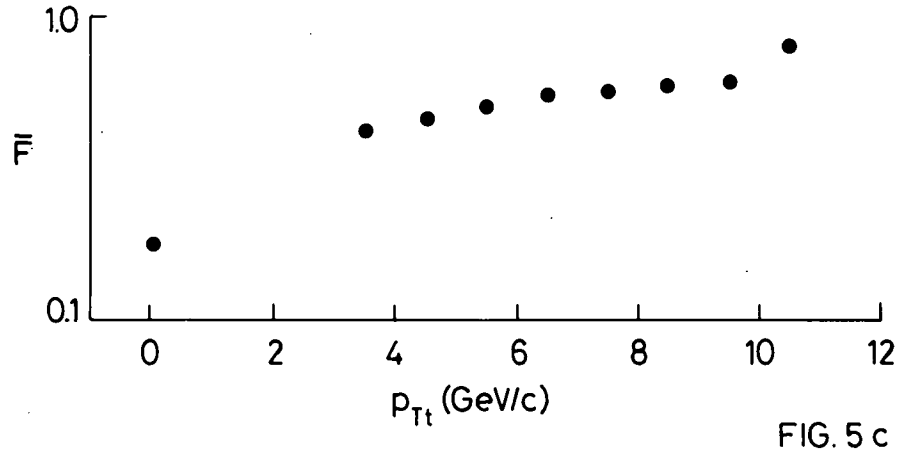

FIG. 5 c

d)

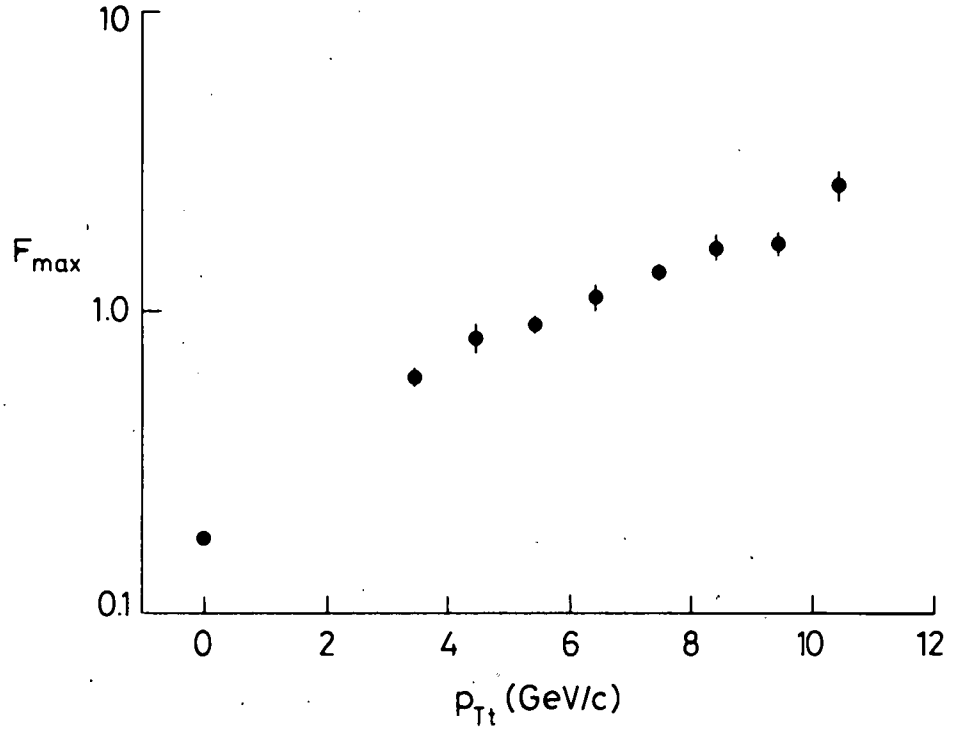

Fig. 5 (c) (d)

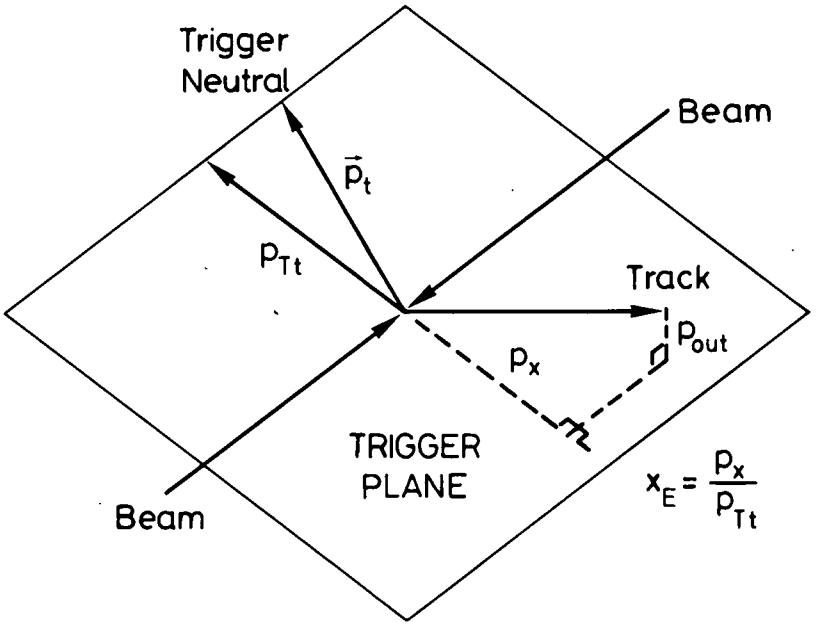
Trigger
Neutral
Beam
$\vec{p}_t$
p_{Tt}
Track
p_{out}
p_x
TRIGGER
PLANE
Beam
$x_E = \frac{p_x}{p_{Tt}}$

Fig. 6

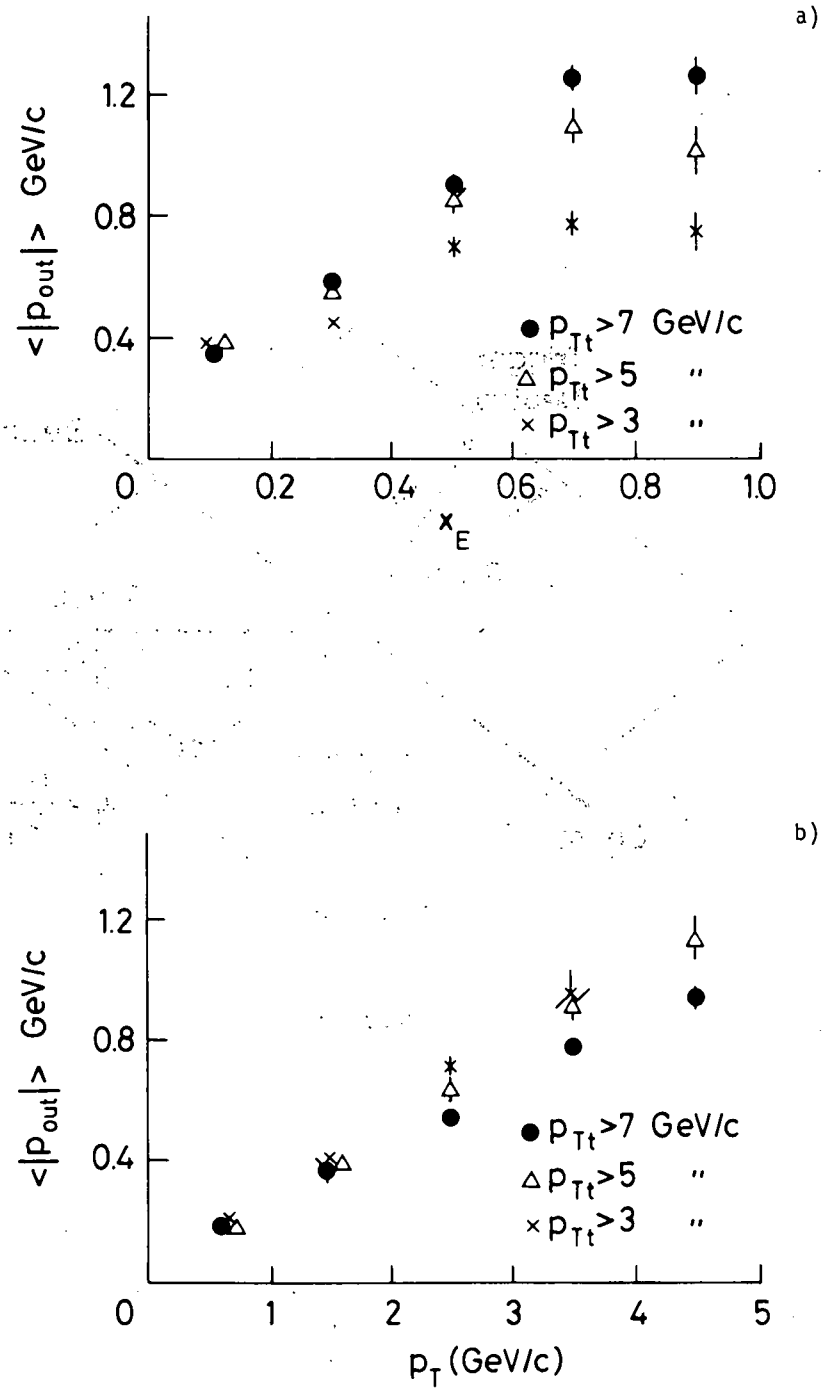
a)
1.2
0.8
0.4
$\langle|p_{out}|\rangle$ GeV/c
p_{Tt}>7 GeV/c
p_{Tt}>5 "
p_{Tt}>3 "
0
0.2
0.4
0.6
0.8
1.0
x_E
b)
1.2
0.8
0.4
$\langle|p_{out}|\rangle$ GeV/c
p_{Tt}>7 GeV/c
p_{Tt}>5 "
p_{Tt}>3 "
0
1
2
3
4
5
p_T (GeV/c)

Fig. 7

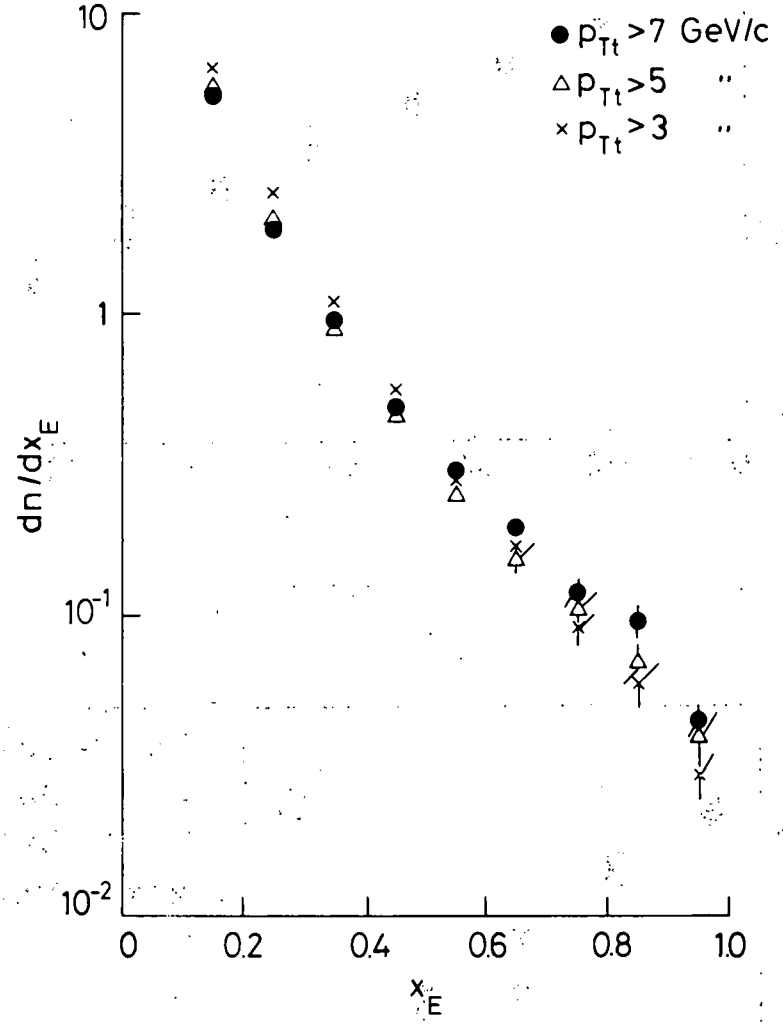

Fig. 8

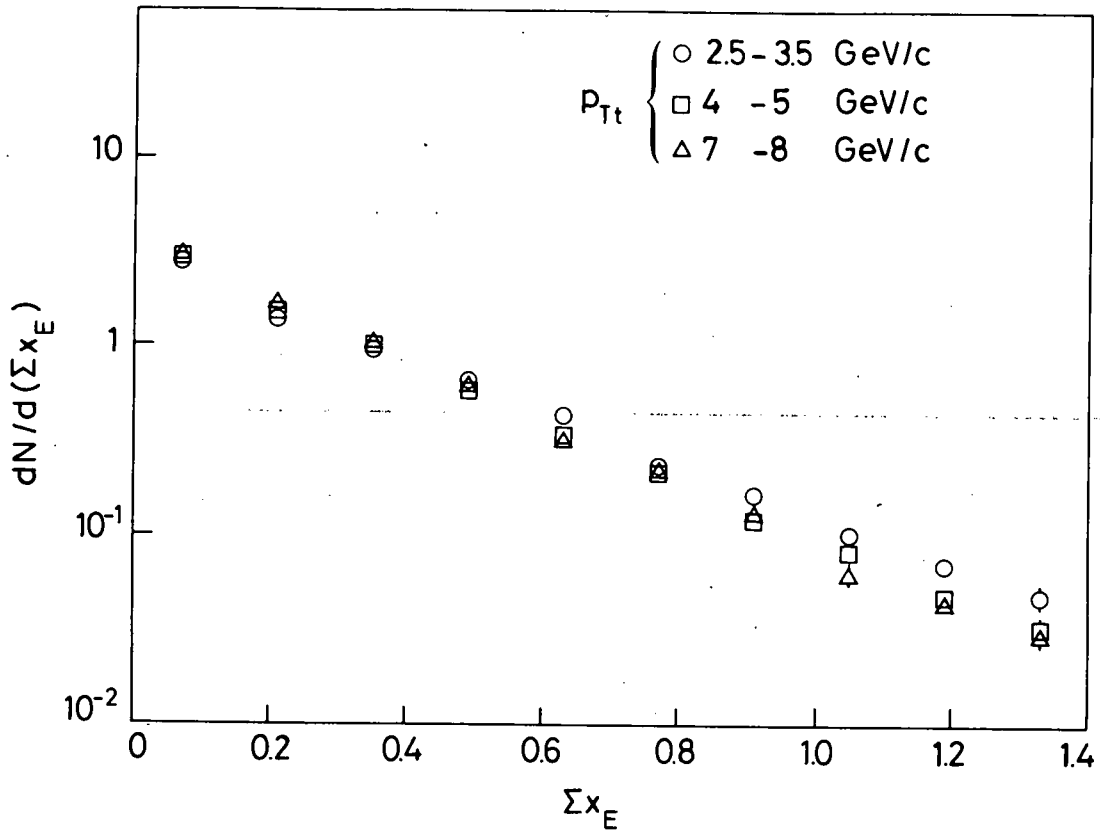
p_{Tt}
○ 2.5-3.5 GeV/c
□ 4 -5 GeV/c
△ 7 -8 GeV/c
10
1
10^{-1}
10^{-2}
$dN/d(\Sigma x_E)$
0
0.2
0.4
0.6
0.8
1.0
1.2
1.4
Σx_E

Fig. 9

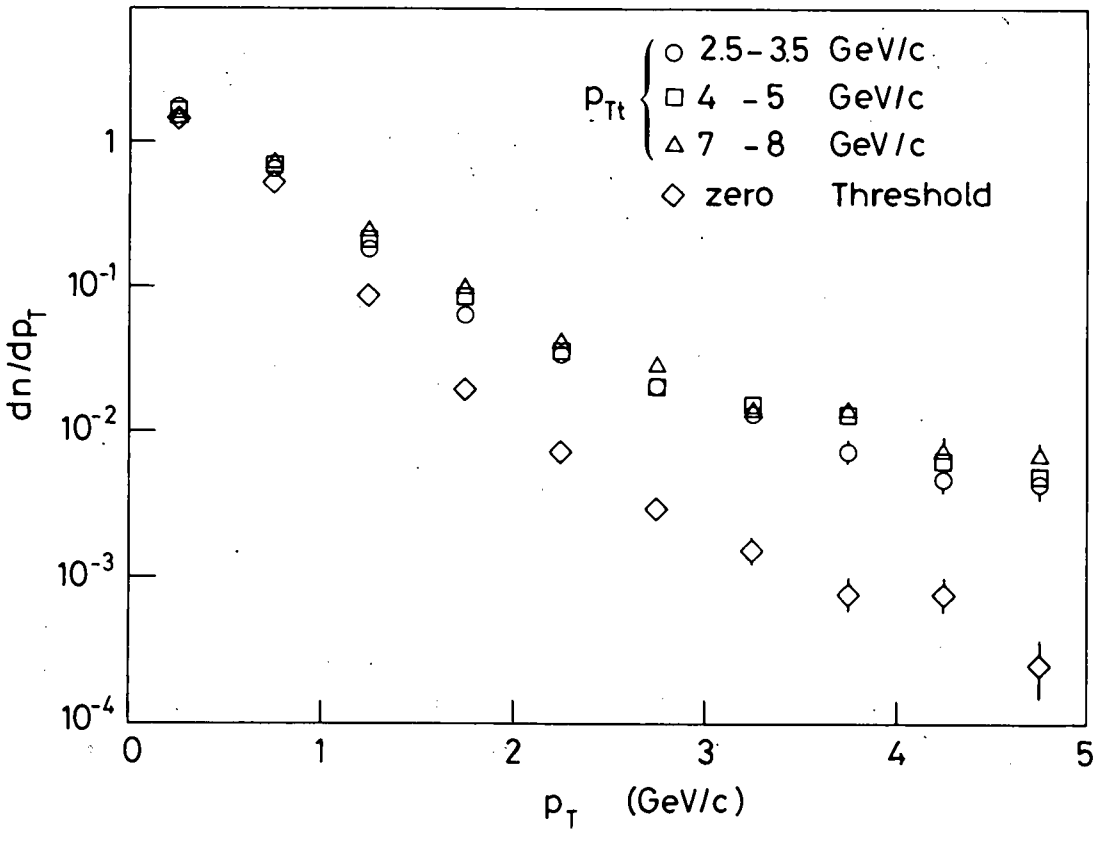
p_{Tt}
○ 2.5-3.5 GeV/c
□ 4 -5 GeV/c
△ 7 -8 GeV/c
◇ zero Threshold
1
10^{-1}
10^{-2}
10^{-3}
10^{-4}
dn/dp_T
0
1
2
3
4
5
p_T (GeV/c)

Fig. 10

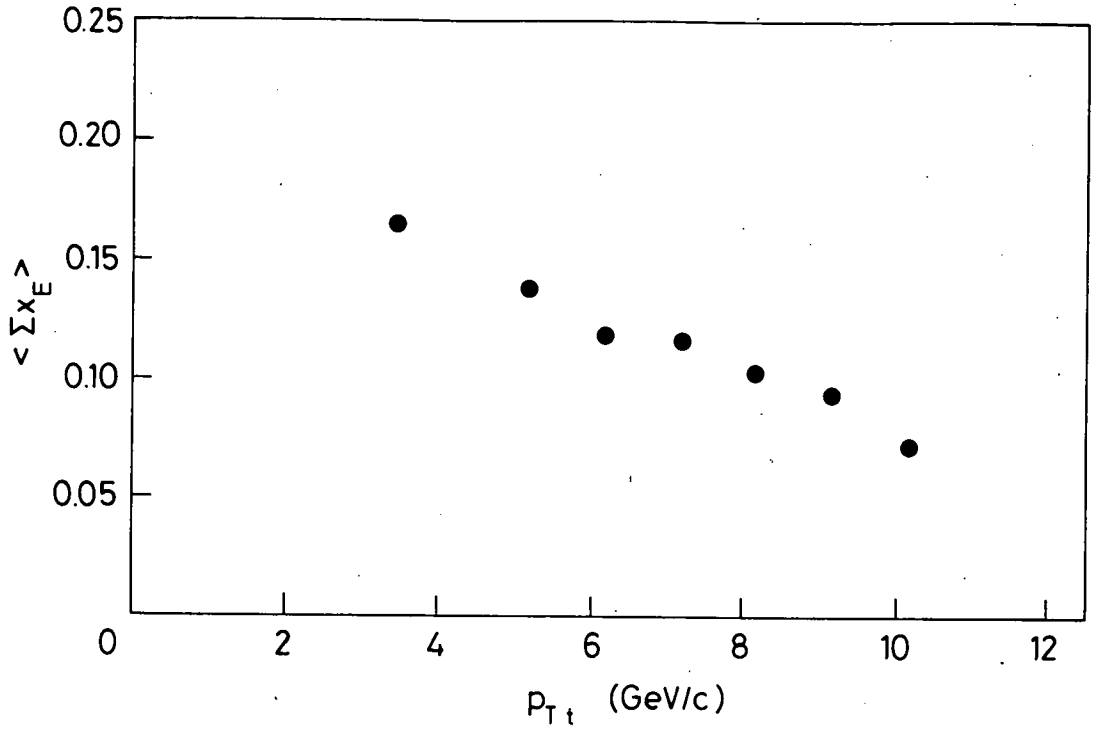
0.25
0.20
0.15
0.10
0.05
0
2
4
6
8
10
12
$\langle \Sigma x_E \rangle$
$p_{T\,t}$ (GeV/c)

Fig. 11

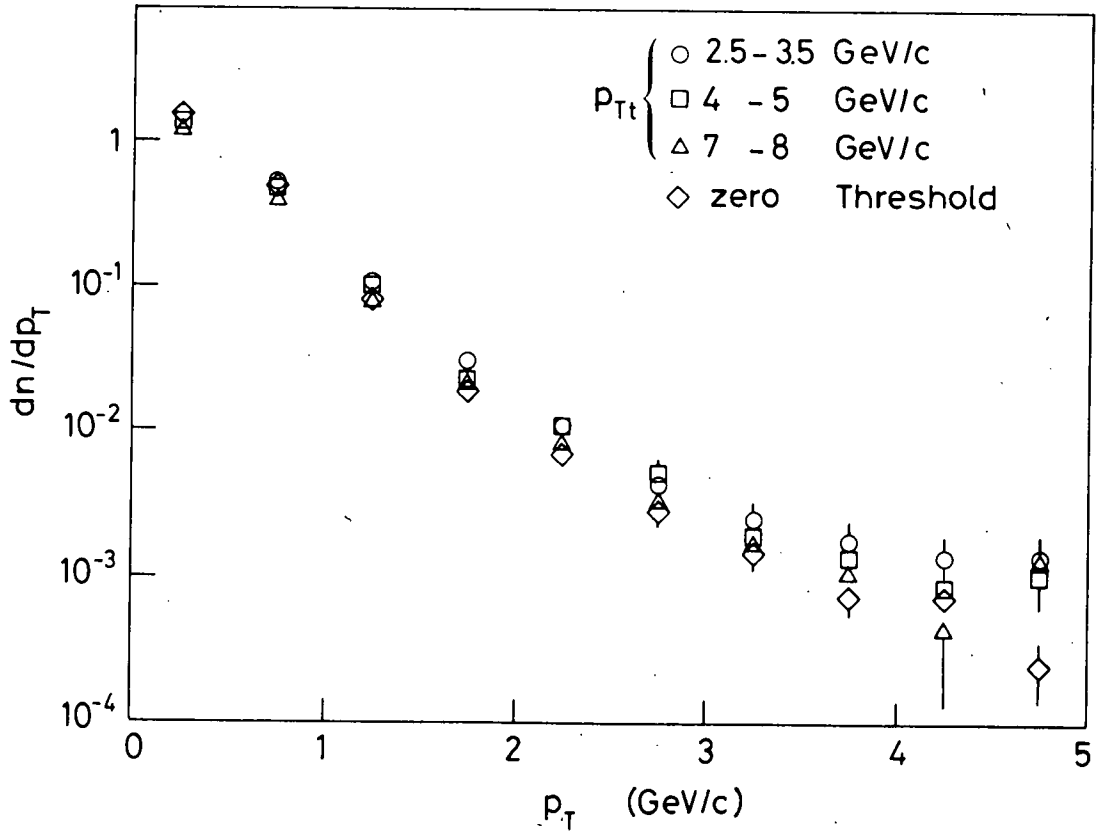
p_{Tt}
○ 2.5 - 3.5 GeV/c
□ 4 - 5 GeV/c
△ 7 - 8 GeV/c
◇ zero Threshold
1
10^{-1}
10^{-2}
10^{-3}
10^{-4}
0
1
2
3
4
5
dn/dp_T
p_T (GeV/c)

Fig. 12

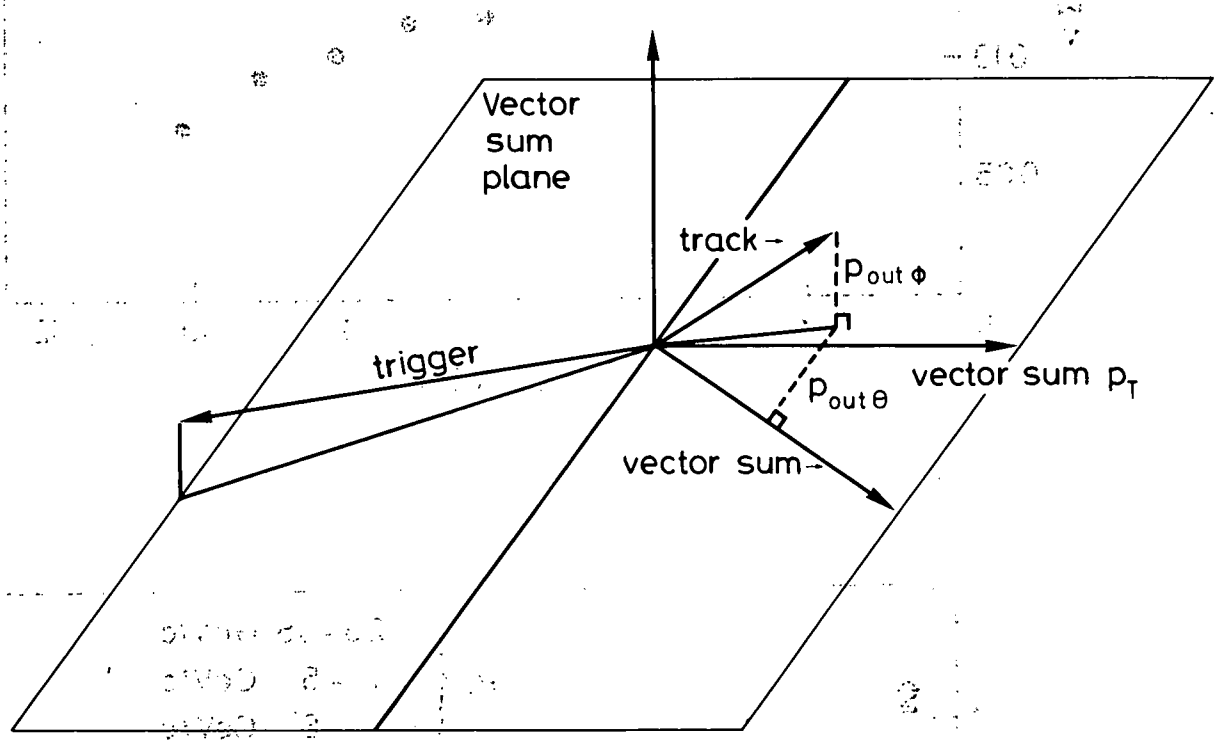
Vector
sum
plane
track
$p_{out\,\phi}$
trigger
vector sum p_T
$p_{out\,\theta}$
vector sum

Fig. 13

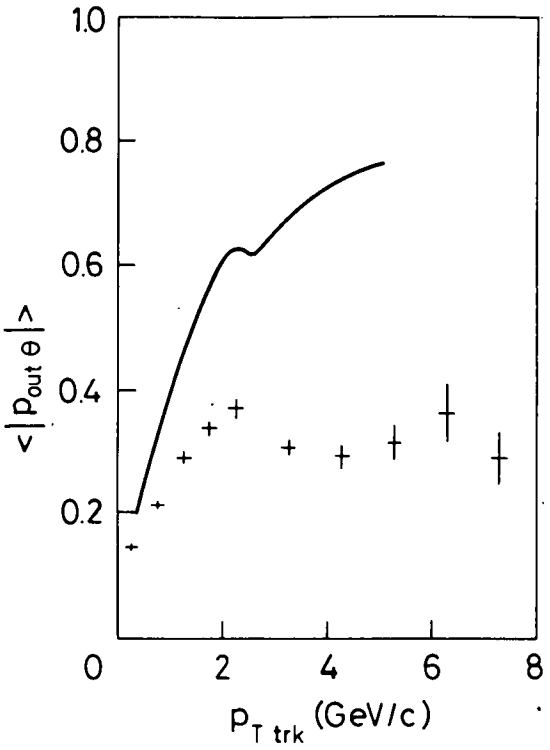
1.0
0.8
0.6
0.4
0.2
0
2
4
6
8
$<|p_{out\,\theta}|>$
$p_{T\,trk}$ (GeV/c)

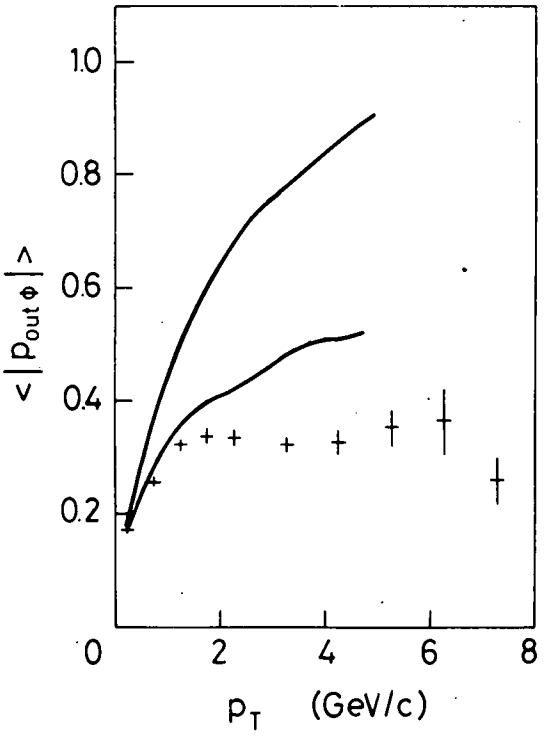
1.0
0.8
0.6
0.4
0.2
0
2
4
6
8
$<|p_{out\,\phi}|>$
p_T (GeV/c)

Fig. 14